Test Statistics for Reflection Symmetry: Applications to Quad-Polarimetric SAR Data for Detection of Man-Made Structures

Paul Connetable, Knut Conradsen, Allan Aasbjerg Nielsen, and Henning Skriver, *Member, IEEE*

***Abstract*—In polarimetric synthetic aperture radar (SAR) images, speckle is removed by multilooking and the local covariance matrix is the main parameter of interest. In the covariance matrix from a backscatter with reflection symmetry, the terms $\langle S_{hh}S_{hv}^{*}\rangle$, $\langle S_{vv}S_{hv}^{*}\rangle$, and their complex conjugates are 0. The backscatter from natural covers, such as fields and forested areas, is typically reflection-symmetric, as these four elements have near-zero values. The backscatter from urban areas and man-made structures is substantially different, and the backscatter from buildings not aligned with the radar line of sight usually does not have reflection symmetry. A novel block-diagonality test statistic for reflection symmetry with a constant false alarm rate property is proposed. It is compared to an approximate test built on a change detection test statistic for Wishart-distributed covariance matrices. Their use on quad-polarimetric data in different situations shows their high potential for man-made structure detection. Applied after an orientation correction of the covariance matrices, these test statistics highlight with high-contrast buildings and urban areas. We also apply this test for ship detection at sea, and show that while the results are unconvincing at X-band, it can also be applied at longer wavelengths such as L-band.**

***Index Terms*—Building detection, radar polarimetry, reflection symmetry, synthetic aperture radar (SAR).**

I. Introduction

TARGET detection and urban area monitoring using polarimetric SAR (polSAR) are important areas of research, due to the all-weather capabilities of SAR and the additional information on ground scatterers brought by polarimetry. Several approaches to target detection have been investigated, for example, by comparing a pixel's value to its surroundings like in cell-averaging constant false alarm (CFAR) methods [1] when using scalar values like the received intensity, or in the polarimetric matching filter [2] when using the whole covariance matrix. Other methods, such as the polarimetric fork [3], compare each pixel to the expected return from a target, or decompose the signal in time–frequency analysis to find scatterers with anisotropic geometric structures [4] which highlight urban areas.

Manuscript received October 1, 2021; revised December 15, 2021 and February 8, 2022; accepted March 22, 2022. Date of publication March 28, 2022; date of current version April 20, 2022. *(Corresponding author: Paul Connetable.)*

Paul Connetable and Henning Skriver are with the National Space Institute, Technical University of Denmark, 2800 Kongens Lyngby, Denmark (e-mail: pjaco@space.dtu.dk; hs@space.dtu.dk).

Knut Conradsen and Allan Aasbjerg Nielsen are with the Department of Applied Mathematics and Computer Science, Technical University of Denmark, 2800 Kongens Lyngby, Denmark (e-mail: knco@dtu.dk; alan@dtu.dk).

Digital Object Identifier 10.1109/JSTARS.2022.3162670

A quad-polarimetric SAR both emits and receives signals in the horizontal and vertical polarizations, denoted h and v, respectively. It measures the relation between the transmitted and the emitted electric fields denoted S_{rt}, where r corresponds to the received polarization and t to the transmitted one. Furthermore, for a monostatic radar and assuming reciprocity, $S_{hv} = S_{vh}$. The covariance matrix is created as the local variance–covariance matrix of the lexicographic vector $\mathbf{k} = [S_{hh}, \sqrt{2}S_{hv}, S_{vv}]$. The covariance matrix is therefore defined as

$$\mathbf{C} = \langle \mathbf{k}\mathbf{k}^{*T} \rangle = \begin{bmatrix} \langle |S_{hh}|^2 \rangle & \sqrt{2}\langle S_{hh}S_{hv}^{*} \rangle & \langle S_{hh}S_{vv}^{*} \rangle \\ \sqrt{2}\langle S_{hv}S_{hh}^{*} \rangle & 2\langle |S_{hv}|^2 \rangle & \sqrt{2}\langle S_{hv}S_{vv}^{*} \rangle \\ \langle S_{vv}S_{hh}^{*} \rangle & \sqrt{2}\langle S_{vv}S_{hv}^{*} \rangle & \langle |S_{vv}|^2 \rangle \end{bmatrix} \quad (1)$$

where $\langle . \rangle$ corresponds to the local average. The reflection symmetry assumption is very common for covariance matrices over natural covers. It implies that the multiple scatterers in a resolution cell have random orientations, and that the backscatter emitted by the resolution cell is symmetric in a plane normal to the SAR line of sight (LOS). It was shown in [5], [6] that reflection symmetry results in no correlation between the co- and cross-polar channels $\langle S_{hh}S_{hv}^{*} \rangle = \langle S_{vv}S_{hv}^{*} \rangle = 0$. The covariance matrix stemming from an reflection symmetric scattering has the form

$$\mathbf{C}_{rs} = \begin{bmatrix} \langle |S_{hh}|^2 \rangle & 0 & \langle S_{hh}S_{vv}^{*} \rangle \\ 0 & 2\langle |S_{hv}|^2 \rangle & 0 \\ \langle S_{vv}S_{hh}^{*} \rangle & 0 & \langle |S_{vv}|^2 \rangle \end{bmatrix}. \quad (2)$$

The model-based decompositions proposed by Alberga *et al.* [7], Freeman and Durden [8], and later, the one proposed by van Zyl in [9] all assume a scattering with reflection symmetry by default. They are widely used, and manage to describe the quad-polarimetric returns based on three basic scattering mechanisms: the odd-bounce, the even-bounce, and volume scatterings. This hypothesis is commonly assumed and accepted for applications related to natural scatterers, such as in [10]. These decompositions are known to perform well over most natural areas, but the reflection symmetry assumption does not hold well over urban areas [11]. The backscatter from buildings aligned with the along-track direction gives a strong double-bounce return, usually with a high intensity, and follows the reflection symmetry assumption. However, this is not true for the

structures not aligned with the along-track direction, or all the parts with slopes, like roofs. In this case, the complex scattering mechanisms contradict the reflection symmetry assumption, and a non-zero return is observed on $\langle S_{hh}S_{hv}^{*}\rangle$ and $\langle S_{vv}S_{hv}^{*}\rangle$.

In this regard, the lack of reflection symmetry can be assessed and used to study urban areas using polSAR. Other model-based decompositions, in particular the Krogager decomposition [12] and the four-elements decomposition introduced by Yamaguchi *et al.* [11] as an extension of the Freeman and Durden decomposition, model the imaginary part of the covariance between the co- and cross-polarization channels as helix scattering. The use of this mechanism drastically improves the performance of decompositions over urban areas. This scattering mechanism can also stem from terrain slopes in natural scenes, but this influence can be corrected for [13]. Some previous work has already shown the importance of investigating the lack of reflection symmetry for detecting large man-made structures. In [14], the direct use of $|T_{23}|$ from the coherency matrix, $|\rho_{rrll}|$, and $|\rho_{hhhv}|$ are compared to detect ships at sea and buildings on ground. In [15], a metric measuring the amount of reflection symmetry is derived, which can be further separated into a helicity and orientation components. Duan *et al.* [16] show that the helix scattering does not fully describe the scattering on urban areas, and that the real parts of $\langle S_{hh}S_{hv}^{*}\rangle$ and $\langle S_{vv}S_{hv}^{*}\rangle$ also contain information which can be used to differentiate buildings and vegetation. The ability of assessing the presence of reflection symmetry in polarimetric images is also of interest for classification purposes [17], [18].

In order to distinguish between man-made and natural targets, a statistical test for reflection symmetry is therefore useful. An *ad hoc* way of doing this is to use the test statistic Q for similarity of two covariance matrices introduced in [19]. The derivation of Q, which was originally used for change detection between data acquired at two time points, is based on the complex Wishart distribution. This adaptation and its shortcomings are described in Section II-A. To avoid these issues, this article introduces in Section II-B a new test statistic Q_{bd} specifically designed to test for block diagonality. In this article, it is applied to test for reflection symmetry, i.e., $\langle S_{hh}S_{hv}^{*}\rangle = \langle S_{hh}S_{hv}^{*}\rangle = 0$. It is associated with a formal distribution, giving this test a CFAR property for rejection of the reflection symmetry hypothesis.

II. Test Statistics

A. Adaptation of the Wishart Change Detection Test Statistic

This section describes the construction of the *ad hoc* test for reflection symmetry. If we denote the covariance matrices $\mathbf{C}$ and the matrices $\mathbf{X} = n\mathbf{C}$ with n being the equivalent number of looks (enl) [20], then the matrices $\mathbf{X}$ are complex Wishart-distributed $\mathbf{X} \sim \mathrm{W_C}(p, n, \mathbf{\Sigma})$, where p is the dimensionality, and $\hat{\mathbf{\Sigma}} = \mathbf{C}$. The test for equality of covariance matrices $\mathbf{C}_0$ and $\mathbf{C}_1$ with $n\mathbf{C}_0 \sim \mathrm{W_C}(p, n, \mathbf{\Sigma}_0)$ and $n\mathbf{C}_1 \sim \mathrm{W_C}(p, n, \mathbf{\Sigma}_1)$ is given in [19], and corresponds to the hypotheses

$$\mathcal{H}_0 : \mathbf{\Sigma}_0 = \mathbf{\Sigma}_1 \text{against}$$

$$\mathcal{H}_1 : \mathbf{\Sigma}_0 \neq \mathbf{\Sigma}_1.$$

This test statistic can be adapted to evaluate if a covariance matrix $\mathbf{C}$ and its reflection symmetric counter-part $\mathbf{C}_{rs}$ are statistically different, where $\mathbf{C}_{rs}$ is obtained by setting to 0 the four components corresponding to the reflection symmetry assumption. In this adaptation, an approximation is made and it is assumed that $\mathbf{X}_{rs} = n\mathbf{C}_{rs}$ is Wishart-distributed, and therefore the comparison is made using the number of degrees of freedom from the full case in [19]. The likelihood ratio test statistic Q is

$$\begin{aligned}\ln(Q) = n[&2p\ln(2) + \ln(\det(\mathbf{X})) + \ln(\det(\mathbf{X}_{rs})) \\ &- 2\ln(\det(\mathbf{X} + \mathbf{X}_{rs}))].\end{aligned} \tag{3}$$

Furthermore, under $\mathcal{H}_0$, $\mathbf{C}$ and $\mathbf{C}_{rs}$ are not statistically different, and the probability of finding a smaller value of $-2\rho\ln(Q)$ is

$$\begin{aligned}P\{-2\rho\ln(Q) \leq z\} \;\simeq\; &P\{\chi^2(f) \leq z\} \\ &+ \omega_2\left[P\{\chi^2(f+4) \leq z\} - P\{\chi^2(f) \leq z\}\right]\end{aligned} \tag{4}$$

with

$$\begin{aligned}f &= p^2 \\ \rho &= 1 - \frac{(2p^2-1)}{6p}\left(\frac{3}{2n}\right) \\ \omega_2 &= \frac{p^2(p^2-1)}{24}\left(\frac{7}{4n^2}\right)\frac{1}{\rho^2} - \frac{p^2}{4}\left(1 - \frac{1}{\rho}\right)^2.\end{aligned} \tag{5}$$

This test statistic for reflection symmetry is an approximation, since it assumes that the two compared covariance matrices are Wishart-distributed with the same dimension, which is not the case. Furthermore, with the test change detection test statistic, for the comparison between two (full polarimetry) $\mathbf{C}$ matrices, the number of degrees of freedom, f, is 9, whereas for the comparison of two matrices with reflection symmetry $\mathbf{C}_{rs}$, the number of degrees of freedom is 5. The *ad hoc* use of Q to test for reflection symmetry, where we compare a $\mathbf{C}$ matrix with a $\mathbf{C}_{rs}$ matrix, readily brings two challenges to mind, namely

1) $\mathbf{C}_{rs}$ does not follow a complex Wishart distribution; and
2) which value should we choose for f?

In particular, this means that this test is not CFAR for reflection symmetry, and its p-values are not uniformly distributed in regions with reflection symmetry.

B. Block-Diagonality of the Covariance Matrix Test

This section introduces the novel test for reflection symmetry. Swapping the second and the third elements in the lexicographic vector $\mathbf{k}$ leads to a reordering of the covariance matrix, which, under the reflection symmetry assumption, becomes

$$\begin{aligned}\mathbf{C} &= \begin{bmatrix} \langle|S_{hh}|^2\rangle & \langle S_{hh}S_{vv}^{*}\rangle & 0 \\ \langle S_{vv}S_{hh}^{*}\rangle & \langle|S_{vv}|^2\rangle & 0 \\ 0 & 0 & \langle|S_{hv}|^2\rangle \end{bmatrix} \\ &= \begin{bmatrix} \mathbf{C}_{11} & \mathbf{0} \\ \mathbf{0} & \mathbf{C}_{22} \end{bmatrix}.\end{aligned} \tag{6}$$

Both $\mathbf{X}_{11} = n\mathbf{C}_{11}$ and $\mathbf{X}_{22} = n\mathbf{C}_{22}$ are Wishart-distributed, $\mathbf{X}_{11} \sim \mathrm{W}_C(2, n, \mathbf{\Sigma}_{x1})$ and $\mathbf{X}_{22} \sim \mathrm{W}_C(1, n, \mathbf{\Sigma}_{x2})$. In the general case, let us denote the off-diagonal matrices $\mathbf{P}$ and

$\mathbf{P}^{*T}$. Testing for reflection symmetry in this case is a block-diagonality test for $\mathbf{C}$. The associated test is

$$\mathcal{H}_0 : \mathbf{P} = \mathbf{0} \text{ against}$$

$$\mathcal{H}_1 : \mathbf{P} \neq \mathbf{0}.$$

Theorem 1: Let the $p \times p$ matrix $\boldsymbol{W}$ be complex Wishart-distributed

$$\boldsymbol{W} \sim W_{\mathbb{C}}(p, n, \boldsymbol{\Sigma})$$

and partitioned into $t \times t$ blocks

$$\boldsymbol{W} = \begin{bmatrix} \mathbf{W}_{11} & \mathbf{W}_{12} & \cdots & \mathbf{W}_{1t} \\ \mathbf{W}_{21} & \mathbf{W}_{22} & \cdots & \mathbf{W}_{2t} \\ \vdots & \vdots & & \vdots \\ \mathbf{W}_{t1} & \mathbf{W}_{t2} & \cdots & \mathbf{W}_{tt} \end{bmatrix}.$$

The diagonal blocks have dimensions $p_\tau \times p_\tau$, $\tau = 1, \ldots, t$, where $\sum p_\tau = p$. We let $\boldsymbol{\Sigma}$ be partitioned similarly, i.e.,

$$\boldsymbol{\Sigma} = \begin{bmatrix} \boldsymbol{\Sigma}_{11} & \boldsymbol{\Sigma}_{12} & \cdots & \boldsymbol{\Sigma}_{1t} \\ \boldsymbol{\Sigma}_{21} & \boldsymbol{\Sigma}_{22} & \cdots & \boldsymbol{\Sigma}_{2t} \\ \vdots & \vdots & & \vdots \\ \boldsymbol{\Sigma}_{t1} & \boldsymbol{\Sigma}_{t2} & \cdots & \boldsymbol{\Sigma}_{tt} \end{bmatrix}.$$

Then,

$$\boldsymbol{W}_{\tau\tau} \sim W_{\mathbb{C}}(p_\tau, n, \boldsymbol{\Sigma}_{\tau\tau}), \quad \tau = 1, \ldots, t.$$

We want to test the hypothesis that the t diagonal components are independent, i.e.,

$$\mathcal{H}_0 : \boldsymbol{\Sigma}_{ij} = \mathbf{0} \text{for} i \neq j$$

$$\mathcal{H}_1 : \exists i \neq j \text{for which} \boldsymbol{\Sigma}_{ij} \neq \mathbf{0}.$$

Under $\mathcal{H}_0$, $\boldsymbol{\Sigma}$ has the form

$$\boldsymbol{\Sigma}_0 = \begin{bmatrix} \boldsymbol{\Sigma}_{11} & \mathbf{0} & \cdots & \mathbf{0} \\ \mathbf{0} & \boldsymbol{\Sigma}_{22} & \cdots & \mathbf{0} \\ \vdots & \vdots & & \vdots \\ \mathbf{0} & \mathbf{0} & \cdots & \boldsymbol{\Sigma}_{tt} \end{bmatrix}.$$

The likelihood ratio test statistic is

$$Q_{bd} = \left(\frac{\det(\boldsymbol{W})}{\prod_{\tau=1}^{t} \det(\mathbf{W}_{\tau\tau})} \right)^n. \tag{7}$$

Furthermore, under $\mathcal{H}_0$, the distribution of $-2\ln(Q_{bd})$ is

$$-2\ln(Q_{bd}) \simeq \chi^2(f) \tag{8}$$

with

$$f = p^2 - \sum_{\tau=1}^{t} p_\tau.$$

For $t = 2$ and 3, and still under $\mathcal{H}_0$, a better approximation is found for the distribution of $-2\rho_{bd}\ln Q_{bd}$

$$P\{-2\rho_{bd}\ln Q_{bd} \leq z\} \simeq P\{\chi^2(f) \leq z\} + \omega_2[P\{\chi^2(f+4) \leq z\} - P\{\chi^2(f) \leq z\}] \tag{9}$$

with

$$\rho_{bd} = 1 - \frac{1}{3n} \frac{p^3 - \sum_{\tau=1}^{t} p_\tau^3}{p^2 - \sum_{\tau=1}^{t} p_\tau^2}$$

$$\omega_2 = \frac{1}{n^2\rho^2} \left[-\frac{1}{36n^2\rho^2} \frac{\left\{p^3 - \sum_{\tau=1}^{t} p_\tau^3\right\}^2}{p^2 - \sum_{\tau=1}^{t} p_\tau^2} + \frac{1}{24n^2\rho^2} \left\{ p^4 - \sum_{\tau=1}^{t} p_\tau^4 \right\} \right]. \tag{10}$$

In other words, high values of $-2\rho_{bd}\ln(Q_{bd})$ are directly linked to a strong likelihood of rejection of $\mathcal{H}_0$ (reflection symmetry). The proof is shown in the Appendix. In the case of the reflection symmetry test with a quad-polarimetric SAR, the ratio test is simply

$$Q_{bd} = \left(\frac{\det(n\mathbf{C})}{\det(n\mathbf{C}_{11})\det(n\mathbf{C}_{22})} \right)^n = \left(\frac{\det(\mathbf{C})}{\det(\mathbf{C}_{11})\det(\mathbf{C}_{22})} \right)^n. \tag{11}$$

C. Threshold Selection

The distributions for both $-2\rho\ln(Q)$ and $-2\rho_{bd}\ln(Q_{bd})$ are known in the case of reflection symmetry and given in (4) and (9), respectively. The critical values corresponding to pixels with no reflection symmetries are high values. The p-values for nonreflection symmetry are obtained as $P = F_0(-2\rho\ln(Q))$ for the Wishart-based test and $P = F_0(-2\rho_{bd}\ln(Q_{bd}))$ for the block-diagonal test, where F_0 is the cumulative distribution function in case of $\mathcal{H}_\prime$. The threshold for detection is determined by using the p-values, and the choice of threshold for a given false alarm rate α is given by $th = F_0^{-1}(1-\alpha)$.

D. Rotations of the Covariance Matrix for Building Detection

Reflection symmetry is orientation-dependent: Structures aligned with the flight line are characterized by a strong double-bounce return, and respect the reflection symmetry assumption. Contrary to this, dihedral scatterers rotated compared to the radar LOS produce a cross-polar return, which is interpreted as volume scattering by the model-based decompositions, such as the one proposed by Freeman and Durden [8], and gives a return on the elements supposed to be null under the reflection symmetry assumption. High values of $-2\rho\ln(Q)$ and $-2\rho_{bd}\ln(Q_{bd})$ are linked to rejection of the reflection symmetry hypothesis, which makes pixels with reflection asymmetry scattering stand out. Therefore, they are able to highlight buildings rotated compared to the radar LOS, but not those aligned with it. We propose to apply rotations to the covariance matrices to make buildings aligned with the radar LOS nonreflection symmetric, so that they can be detected as well with the proposed reflection symmetry tests.

Information about the orientation of objects compared to the radar LOS is contained in the covariance matrix [13], and can be used in this situation. A rotation of angle θ around the radar LOS is applied to the covariance matrix $\mathbf{C}$ by [21]

$$\mathbf{C}(\theta) = \mathbf{U}(\theta)\mathbf{C}\mathbf{U}^T(\theta) \tag{12}$$

with

$$\mathbf{U}(\theta) = \frac{1}{2} \begin{bmatrix} 1 + \cos(2\theta) & \sqrt{2}\sin(2\theta) & 1 - \cos(2\theta) \\ -\sqrt{2}\sin(2\theta) & 2\cos(2\theta) & \sqrt{2}\sin(2\theta) \\ 1 - \cos(2\theta) & -\sqrt{2}\sin(2\theta) & 1 + \cos(2\theta) \end{bmatrix}. \tag{13}$$

The orientation angle is defined as the angle θ which maximizes the copolarization response [13], which also corresponds to the angle which minimizes the cross-polarization response, i.e., the middle term of the covariance matrix $\mathbf{C}_{22}(\theta)$ after rotation. The results from model-based decompositions are dependent on the orientation of structures on the ground compared to the radar of sight. The correction for the orientation angle is often used before applying these decompositions, as in [21], which greatly improves the results over urban areas, since the cross-polar return from dipoles rotated compared to the radar LOS is correctly interpreted as double-bounce instead of volume scattering. This rotation also compensates the influence of terrain slopes on the scattering [22]. The estimate of the orientation angle $\hat{\theta}$ using the circular polarization algorithm is [13]

$$\tan(4\hat{\theta}) = \frac{-2\mathcal{R}e\left(\langle S_{hv}^{*}(\frac{S_{hh}-S_{vv}}{2})\rangle\right)}{\langle|\frac{S_{hh}-S_{vv}}{2}|^2 - |S_{hv}|^2\rangle}. \tag{14}$$

Correcting for this angle rotates the data such that the ground scatterers appear aligned with the radar LOS, which also minimizes the nonreflection symmetric behavior of objects behaving like dihedral scatterers. To detect man-made structures using the reflection symmetry detectors, an additional rotation needs to be performed after correcting for the orientation angle, so that all scatterers appear as if they were slightly rotated compared to the radar LOS. This operation makes the scatterers with a strong double-bounce return non-reflection symmetric again, which in turn makes them detectable by the reflection symmetry test statistics. This can be modeled by adding a constant bias angle θ_b to the orientation angle. Therefore, a rotation of value $-\hat{\theta} + \theta_b$ is applied to every pixel, with $\hat{\theta}$ obtained using (14). The orientation angle estimate $\hat{\theta}$ is a local value, calculated on each pixel, while the bias is a small uniform value. The value of θ_b for building detection can be chosen experimentally based on a signal-to-noise ratio study.

E. Circular Polarization

The transformation from the linear to the circular basis is done with [13]

$$\begin{aligned} S_{rr} &= (S_{hh} - S_{vv} + 2iS_{hv})/2 \\ S_{ll} &= (S_{vv} - S_{hh} + 2iS_{hv})/2 \\ S_{rl} &= i(S_{hh} + S_{vv})/2. \end{aligned} \tag{15}$$

The correlation coefficient ρ_{rrll} is regularly used for studies on urban areas and man-made structures. It is defined as

$$\rho_{rrll} = \frac{\langle S_{rr}S_{ll}^{*}\rangle}{\sqrt{\langle S_{rr}S_{rr}^{*}\rangle\langle S_{ll}S_{ll}^{*}\rangle}}. \tag{16}$$

The block-diagonal algorithm can also be used to test whether $\rho_{rrll} = 0$ within the 2-by-2 covariance matrix

$$\mathbf{C}_{rl} = \begin{bmatrix} \langle S_{rr}S_{rr}^{*}\rangle & \langle S_{rr}S_{ll}^{*}\rangle \\ \langle S_{rr}^{*}S_{ll}\rangle & \langle S_{ll}S_{ll}^{*}\rangle \end{bmatrix}.$$

III. Applications to Quad-Polarimetric SAR Data

A. Vejers

The first dataset used to demonstrate these tests was acquired with the airborne F-SAR from the German Aerospace Center (DLR) for the Danish Ministry of Defence Acquisition and Logistics Organization (DALO) during a campaign in June 2017. The area shown in the examples below is a part of Vejers, a small town located in the western part of Denmark. In X-band, the pixel spacing is 15 cm both in range and azimuth, and the processed resolution is 25 by 29 cm in azimuth and range, respectively. In L-band, the pixel spacing is 30 by 60 cm in azimuth and range, respectively, and the processed resolution is 60 by 129 cm in azimuth and range, respectively.

An RGB representation of the studied area in X-band is shown Fig. 1, using the decomposition proposed by van Zyl [9]. It is a suburban area, with cottages surrounded by small gardens. The properties are typically separated by trees and hedges, whose backscatter is dominated by volume scattering. A camping site with parking spaces for caravans is situated below the main road which cuts the image into two. Two colored rectangles highlight zones of interest, which are shown more in detail later.

The choice of θ_b is important, as it is an arbitrary value which influences greatly the capacity of the reflection symmetry tests to detect man-made structures after the orientation angle correction. A contrast study was performed on the Vejers dataset acquired with the F-SAR by selecting all the pixels of a building aligned with the radar LOS to represent a target, and pixels over a natural area to represent the background, with the measure

$$Co(\theta_b) = 10\log_{10}\left\{Y_{ta}(\theta_b)/Y_{bg}(\theta_b)\right\} \tag{17}$$

where $Y_{ta}(\theta_b)$ is the 99th percentile of the $-2\rho\ln(Q)$ values for the Wishart-based test, of the $-2\rho_{bd}\ln(Q_{bd})$ values for the block-diagonal test, and of $|\rho_{rrll}|$ over selected the buildings. Likewise, $Y_{bg}(\theta_b)$ is the 99th percentile of the same values over the background. In X-band, the selected background is a grass field. Similarly, a contrast study was performed in L-band using pixels from several houses as targets and a forested area as background. The results of the contrast study are shown in Fig. 2. The results are almost symmetric around 0, and the best contrast values are found in the interval $[-3\pi/32, -\pi/16]$ and, with slightly lower values, in $[\pi/16, 3\pi/32]$. The lack of symmetry around 0 in the contrast study is most likely due to the fact that a single building was used to select all the target pixels. In the rest of the study, $\theta_{\text{bias}} = \pi/16$ is used for both wavelengths.

The results obtained by applying the two reflection symmetry tests on the scene, before applying rotations to the covariance matrices, are presented in the top row of Fig. 3. The values of $-2\rho\ln(Q)$ (Wishart change detection-based test statistic) over the area are shown on the left, and the values of $-2\rho_{bd}\ln(Q_{bd})$ (block-diagonal test statistic) on the right. Most buildings are well highlighted by both reflection symmetry test statistics, which are also able to highlight the caravans in the camping site. However, several structures aligned with the radar LOS, most notably the cottages in the area delimited by the red rectangle, are not highlighted by these tests. The bottom row of Fig. 3 shows on the left the values of $-2\rho_{bd}\ln(Q_{bd})$ from

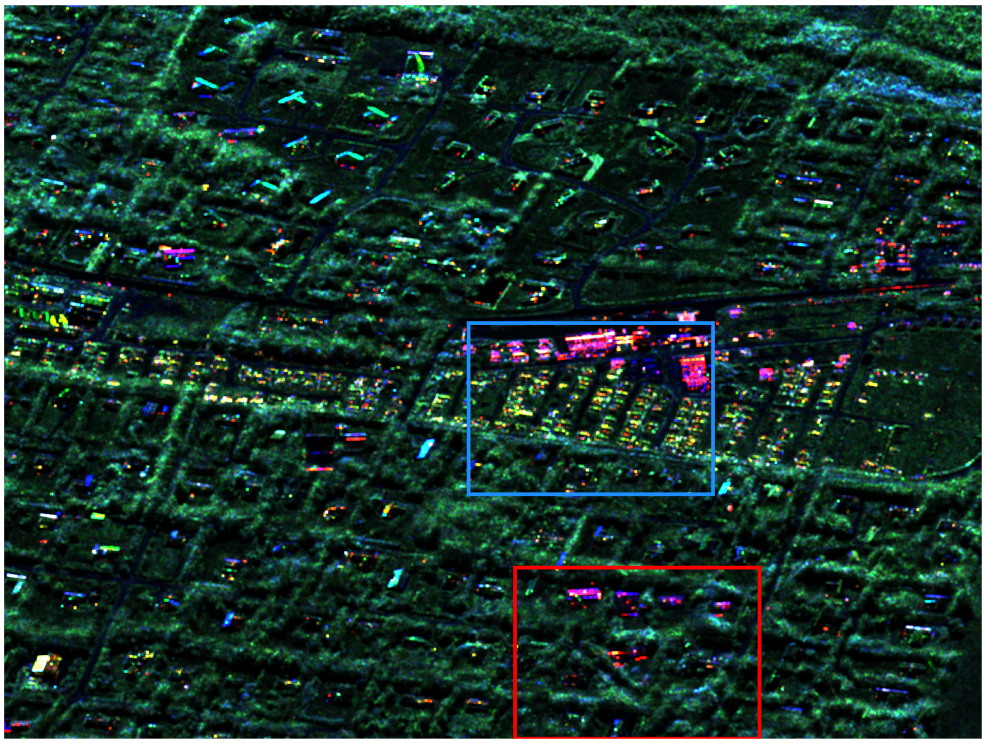

Fig. 1. van Zyl decomposition over a part of Vejers, acquired by the F-SAR in X-band. The red, green, and blue channels show the power explained by the even-bounce, the remainder, and the odd-bounce according to the decomposition, respectively.

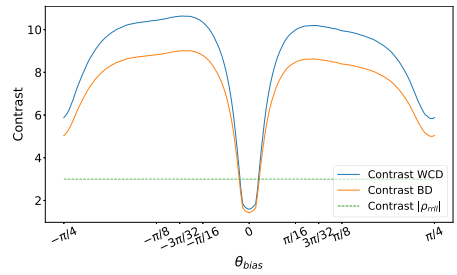

(a)

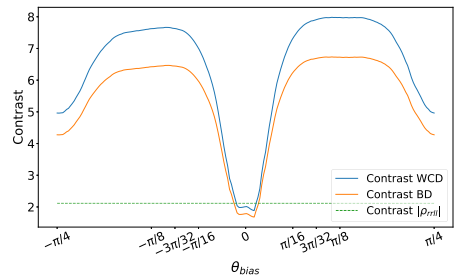

(b)

Fig. 2. Signal-to-noise ratio study as a function of the bias angle θ_b, for X-band in (a) and for L-band in (b), both over Vejers. The values are obtained using (17). The blue line represents the contrast for the Wishart change detection-based test, the orange line the contrast for the block-diagonality test, and the green dashed line represents the contrast obtained by $|\rho_{rrll}|$. (a) Contrast at X-band, logarithmic scale. (b) Contrast at L-band, logarithmic scale.

the block-diagonal test after applying the orientations described earlier, and $|\rho_{rrll}|$ on the right. After rotation of the covariance matrices, the $-2\rho_{bd}\ln(Q_{bd})$ values have risen over buildings when compared to Fig. 3(b), while the noise on the background stayed similar. The detection obtained with a false alarm rate $\alpha = 10^{-3}$ with the block-diagonal test statistic after applying the proposed rotations to the covariance matrices is shown in Fig. 4.

The contrast as defined in (17) between buildings and forested areas went from around 4 before the rotations to more than 5.5 after, for the block-diagonal test statistic. Furthermore, several structures which are not or badly highlighted before the rotations are very apparent, such as the cottages in the red rectangle area, or buildings in the top of the blue rectangle area. The values of $|\rho_{rrll}|$ in 3(d) show that this correlation coefficient highlights structures similar to the reflection symmetry tests, with a higher noise on the background than the test statistics, as highlighted in Fig. 2.

The two test statistics give similar results, as is further seen in the scatter plot on the left of Fig. 5. The main difference between the two algorithms comes from the difference of number of degrees of freedom for the χ^2 distribution in case of reflection symmetry, which changes the obtained p-values, as shown in the right side of Fig. 5. In both cases, the scatter plots form lines and not cloud points, indicating the existence of a function linking the test statistic values from the two tests, as well as the p-values.

The area in the red rectangle in Fig. 1 contains several cottages, of which several are aligned with the radar LOS, and for which the double-bounce scattering is dominant. The corresponding zoomed version is shown in Fig. 6, along with $-2\rho_{bd}\ln(Q_{bd})$ values before [Fig. 6(c)] and after [Fig. 6(d)] covariance matrix rotations, as well as with $|\rho_{rrll}|$ values [Fig. 6(e)]. In the Google Earth image [Fig. 6(a)], it can be seen

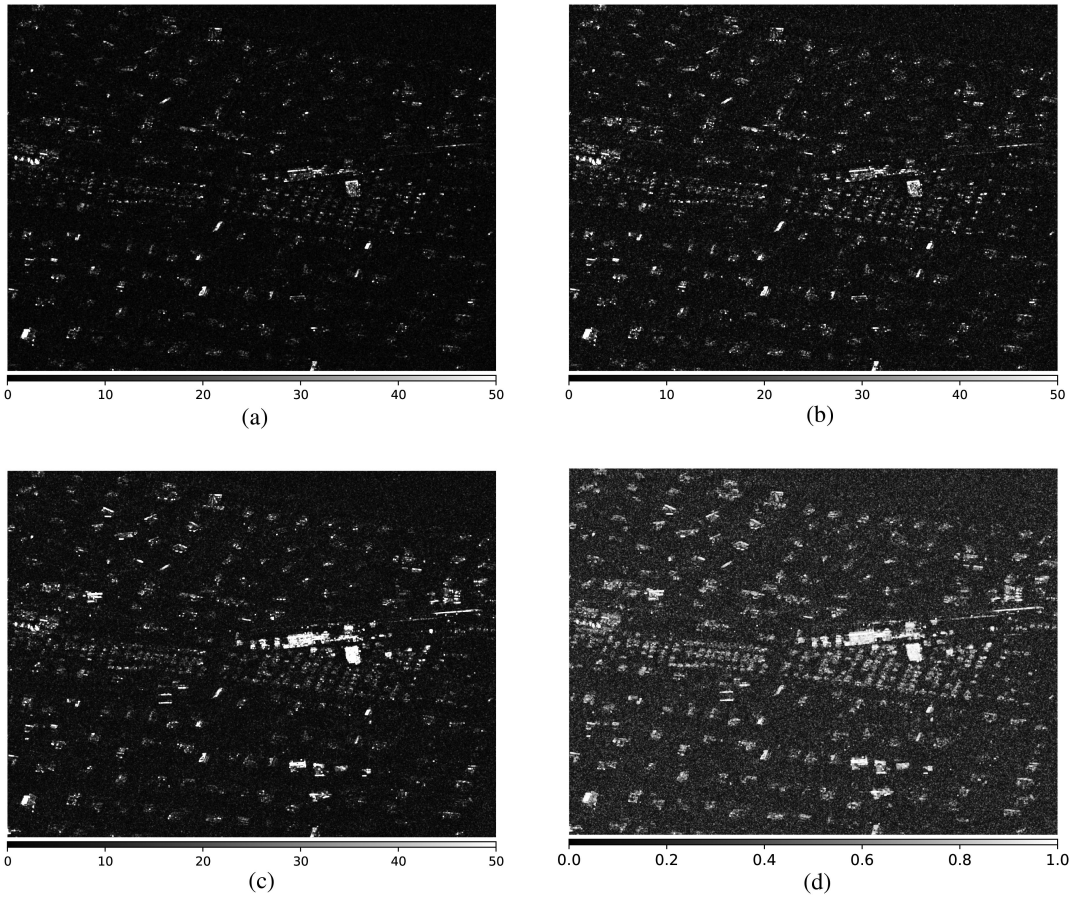

Fig. 3. (a) $-2\rho\ln(Q)$. (b) $-2\rho_{bd}\ln(Q_{bd})$ before any rotations of the covariance matrices. (c) $-2\rho_{bd}\ln(Q_{bd})$ after rotation of the covariance matrices. (d) $|\rho_{rrll}|$.

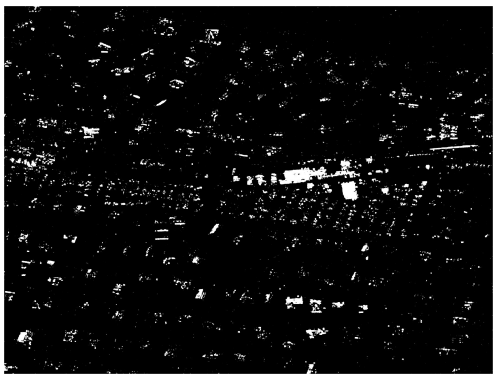

Fig. 4. Detection result obtained with the false alarm rate $\alpha = 10^{-3}$ on the covariance matrices after correcting for the orientation angle with a bias, with the block-diagonal test statistic, at X-band.

that the cottages form three horizontal rows. The comparison between Fig. 6(c) and (d) shows that the cottages which are not or barely apparent before rotating the covariance matrices are highlighted well by the reflection symmetry detectors after the rotations. Despite the clear improvement, the cottage on the right of the middle row and the two cottages on the left of the bottom row are still difficult to see in Fig. 6(d), though for each of them, a few pixels have values significantly higher than the background. These cottages do not appear either in the RGB van Zyl decomposition, and look like they are hidden by vegetation, which makes them harder to distinguish from natural background.

The area in the blue rectangle in Fig. 1 is shown more in detail in Fig. 7. In the top of the area, several buildings and caravans are aligned with the radar LOS, and are characterized by a strong double-bounce scattering, appearing in red in the van Zyl decomposition [Fig. 7(b)]. These structures, especially the caravans on the left, are not highlighted well before covariance matrix rotation Fig. 7(c), and are detected way better by the same test after the proposed rotations are applied to the covariance matrices [Fig. 7(d)]. For example, the contrast between the leftern-most caravan and the grass background rises from 3.3 to 8.8 after applying the covariance matrix rotations, for the block-diagonal test statistic. Additional caravans with a different orientation cover most of the rest of the area. They appear in white in the Google Earth image [Fig. 7(a)], and are easy to distinguish in the van Zyl decomposition, due to the relatively high intensity of the backscatter compared to the ground. They appear mostly in colors which range from green to yellow, indicating that the volume scattering plays an important role on the caravans' backscatter. There are also several red pixels, indicating that double-bounce scattering is dominant in some specific parts of the caravans or their surroundings. These bright

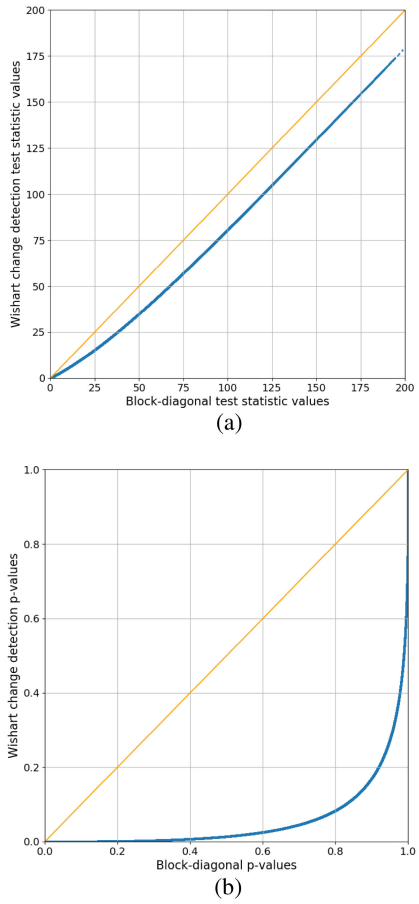

Fig. 5. Comparison of the two tests presented. In (a), $-2\rho \ln(Q)$ values of the two tests are shown as a function of $-2\rho_{bd} \ln(Q_{bd})$. The values are extremely close and correlated. In (b), the same type of plot is shown for the *p*-values, and shows that the different degrees of freedom between the two tests changes quite a lot the behavior of the *p*-values. (a) Test statistic values. (b) *p*-Values

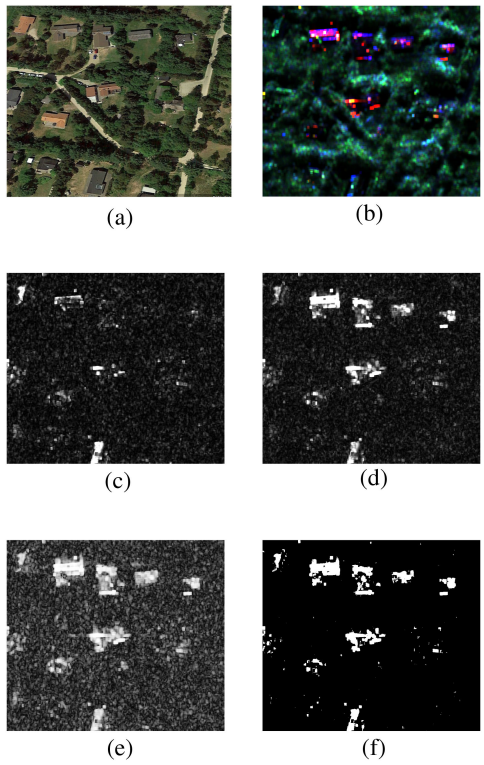

Fig. 6. Zoomed version of the area in the red rectangle. (a) Satellite image of the area, from Google Earth. (b) van Zyl decomposition. (c) $-2\rho_{bd} \ln(Q_{bd})$, before orientation correction. (d) $-2\rho_{bd} \ln(Q_{bd})$, after orientation correction. (e) $|\rho_{rrll}|$. (f) Detection obtained with a false alarm rate $\alpha = 10^{-3}$ with the block-diagonal test statistic after rotation of the covariance matrices.

spots can, for example, be cars, which are usually parked close to the caravans. The values of $-2\rho_{bd} \ln(Q_{bd})$ over the caravans are similar after rotation of covariance matrices [Fig. 7(d)], and are easily distinguishable from the background. The rectangular building in red in the top right part of the area is a brick building. The scattering happening on the roof of this building is dominated by double-bounce, though the building itself is not aligned with the along-track direction. A closer inspection shows that its roof is covered with several rows of skylights and a row of solar panels. The top row of skylights has a backscatter, including some volume scattering, as can be seen by their yellow color, since they are not aligned with the radar LOS. A part of the roof has a backscatter dominated by single-bounce scattering and appears in blue. This building is already clearly highlighted in Fig. 7(c) before rotating the covariance matrices, but this rotation in Fig. 7(d) brings higher values and a better spatial togetherness. The contrast between this building and a grass background rises from 8.0 to 10.6 after applying the rotations to the covariance matrices, and using the block-diagonal test statistic. As expected, the top row of skylights, which behave like tilted double-bounce scatterers, stands out the most before the rotations are applied.

The reflection symmetry detectors also highlight buildings well at L-band. The studied area in L-band shown in Fig. 8 covers the same part of Vejers, and is larger than the one at X-band. The top right part of the scene is a forested area, the bottom right part covers the area studied in X-band, while the left part of the image contains more built areas with cottages. Both the Wishart change detection-based test statistic [Fig. 8(b)] and the block-diagonal test statistic [Fig. 8(c)] show a clear map of buildings over the urban areas, and have low noise over the forested area. As a comparison, $|\rho_{rrll}|$ in Fig. 8(d) highlights similar structures, albeit with more noise in the background. Furthermore, the detection obtained with a false alarm rate $\alpha = 10^{-3}$ with the bloc-diagonal test statistic on the covariance matrices after rotation is shown in Fig. 9.

B. Coastal Area

A second dataset is used to illustrate the behavior of the reflection symmetry tests over water. It was acquired as well with the F-SAR by DLR for DALO, as part of another campaign in October 2014, over Sjaellands Odde, Denmark. The data shown were acquired in X-band, with the same resolutions as described for the Vejers area.

The van Zyl decomposition of the studied area is shown in Fig. 10(a). It consists of a stripe of land, with a grass field, and a few buildings on the right. The land is surrounded by water, in black, both on the top and the bottom parts of the scene. Four

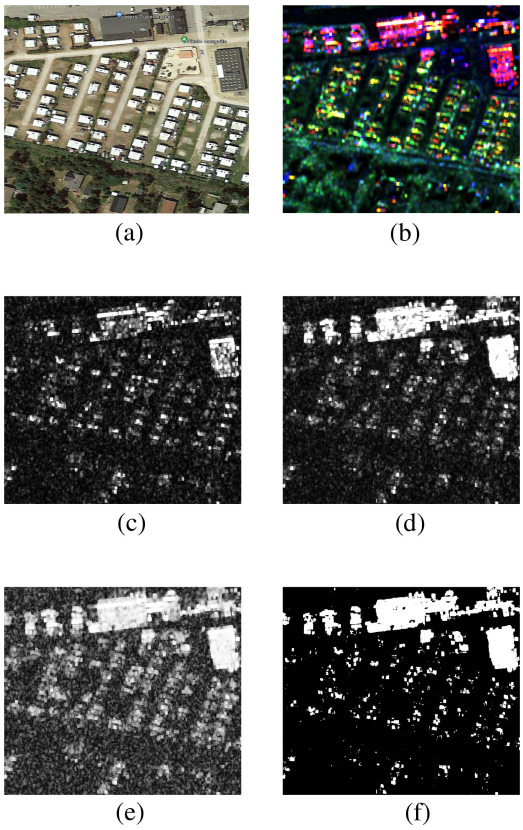

Fig. 7. Zoomed version of the area in the blue rectangle. (a) Satellite image of the area, from Google Earth. (b) van Zyl decomposition. (c) $-2\rho_{bd}\ln(Q_{bd})$, before orientation correction. (d) $-2\rho_{bd}\ln(Q_{bd})$, after orientation correction. (e) $|\rho_{rrll}|$. (f) Detection obtained with a false alarm rate $\alpha = 10^{-3}$ with the block-diagonal test statistic after rotation of the covariance matrices.

boats were placed at sea, in the bottom of the image, and appear very clearly in the van Zyl decomposition as bright red dots. The values obtained with block-diagonal test statistic $-2\rho_{bd}\ln(Q_{bd})$ after rotation of covariance matrices are shown in 10(b). The test statistic manages very well to highlight the buildings on land, but behaves differently on water. The water does not appear to follow the reflection symmetry assumption at X-band, while the boats, which appear in dark, do. This happens because of the roughness of the sea surface at X-band. The results are similar for $|\rho_{rrll}|$. In these conditions, the reflection symmetry detectors are therefore badly suited for boat detection, and so is $|\rho_{rrll}|$, as it was already reported in [14].

C. San Francisco

Finally, the test statistics are also applied to a quad-polarimetric image of San Francisco, acquired in L-band by the PALSAR-2 instrument aboard the satellite ALOS-2. It was acquired in March 2015, in the high-sensitive mode with quad-polarimetry (HBQ), with a ground resolution of 6-by-6 m.

San Francisco is a commonly studied area in polarimetric SAR imaging, thanks to its great variety of scatterers. In particular, it contains several urban grids with different orientations, which give very different polarimetric backscatters with a SAR sensor. It also features a park, golf courses, bridges, and open water with ships sailing regularly. The area is shown in RGB colors in the top left image of Fig. 11, using the natural logarithms on the powers obtained with the van Zyl decomposition. A part of the Golden Gate bridge can be seen on the top of the image, which coincides to the North direction. The bridge which goes toward the East is the Oakland Bay bridge. The urban area connected to this bridge in San Francisco is the known as the South Of Market Area (SOMA), and is titled by around $45°$ compared to the radar LOS and the other urban grids. This orientation creates a high return on the cross-polar channel, which is analyzed as volume scattering by the decomposition, hence the vivid green color of the area. Furthermore, the area is densely built. Blasco *et al.* [23] demonstrate that for urban areas, and more particularly in this case for rotated urban areas, the height of buildings, the width of streets, and the structure of the roofs also play an important role in the scattering. Here, the return observed in the SOMA is complex and cannot only be explained by rotated double-bounce.

Just North of SOMA, a large urban grid appears in red and blue, which contains several districts. We refer to it loosely as the city-center area. This area is well aligned with the satellite flight path, and is densely built as well. The other built areas are slightly rotated compared to radar LOS, are less densely built, and are composed of smaller buildings than the SOMA and the city center. The backscatter in these areas contains both double-bounce and volume scattering, which particularly stands out in yellow in the van Zyl decomposition. Finally, four ships sailing at the time of the acquisition are visible, two on the top right corner (East of Treasure Island), and two others near the bottom right corner of the scene.

The top right image of Fig. 11 shows the values $-2\rho_{bd}\ln(Q_{bd})$ obtained with the block-diagonal test statistic, before any rotations are applied to the covariance matrix. Under this circumstance, the reflection symmetry test highlights structures rotated relatively to the radar LOS. Unsurprisingly, the structures in the city center are therefore not highlighted. All the other urban grids are well detected, and in particular, the SOMA buildings are easy to see. The highest values are obtained on a triangular area to the North-West of the city, which appeared in yellow in the van Zyl decomposition. Finally, the four boats are clearly distinguishable in the water, though one has slightly lower values than the others.

The bottom left image of Fig. 11 also shows the values of $-2\rho_{bd}\ln(Q_{bd})$, after rotation of the covariance matrices. It is similar to the image in the bottom left corner, which shows the values of $|\rho_{rrll}|$ over the same area. All the urban areas are highlighted and clearly delineated, with the notable exception of SOMA. Some docks on the North-East part of the city also have low values after rotation, while they were detected prior rotations to the covariance matrix in Fig. 11(b). These docks also appeared with a strong volume contribution to the scattering in the van Zyl decomposition. This happens because the scattering happening on these areas is not simply the result from rotated dihedrals, but are more complex, and probably also contain contributions from rotated trihedrals, as well as other components [23]. In contrast, the values of $-2\rho_{bd}\ln(Q_{bd})$ over the water have slightly increased after rotation of the covariance

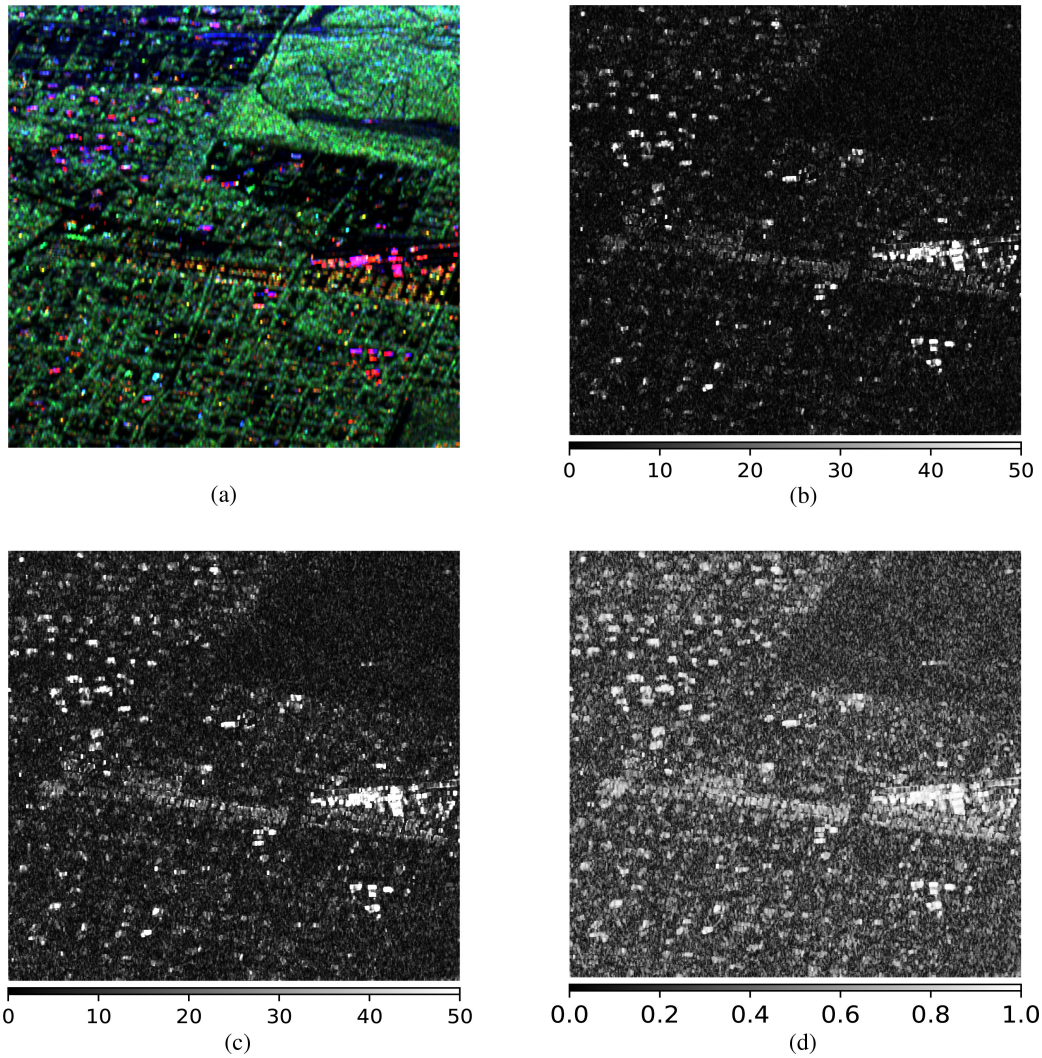

Fig. 8. Scene acquired in L-band with the F-SAR over Vejers. (a) Van Zyl decomposition. The RGB channels correspond to the power explained by, respectively, the even-bounce, the remainder, and the odd-bounce components of the decomposition. (b) $-2\rho\ln(Q)$ after applying the rotations to the covariance matrix. (c) $-2\rho_{bd}\ln(Q_{bd})$ after applying the rotations to the covariance matrix. (d) $|\rho_{rrll}|$.

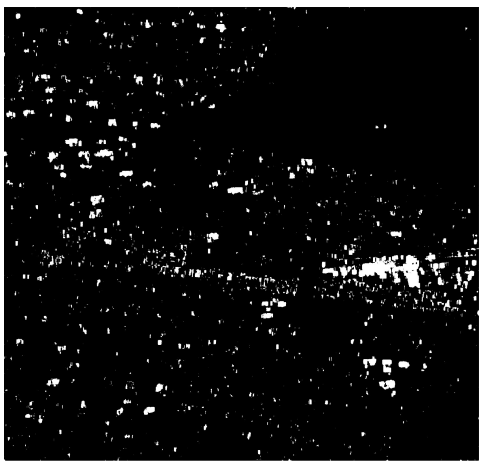

Fig. 9. Detection result obtained with the false alarm rate $\alpha = 10^{-3}$ on the covariance matrices after correcting for the orientation angle with a bias, for the block-diagonal test statistic, at L-band.

matrices, decreasing the contrast between ships and water in the bottom right corner. The four pylons of the Oakland bay bridge, which is the bridge to the right of the image, can be identified in Fig. 11(c) with the bright zones along the bridge.

These observations show that when buildings are rotated with a large azimuth angle in urban areas, the observed scattering cannot always be explained as rotated double-bounce, as for the SOMA. In this case, the tests for reflection symmetry applied after rotation of covariance matrices to correct for the orientation angle with a bias do not always highlight these rotated buildings. Likewise, without these rotations, the tests do not highlight buildings aligned with the radar LOS. The information brought by this test in both cases is relevant. The combined use of the test statistic before and after applying rotations to covariance matrices can detect both buildings aligned and not aligned with the radar LOS. The detections obtained with a false alarm rate $\alpha = 10^{-3}$ on the San Francisco area using the block-diagonal test statistic, both before and after applying rotations to the

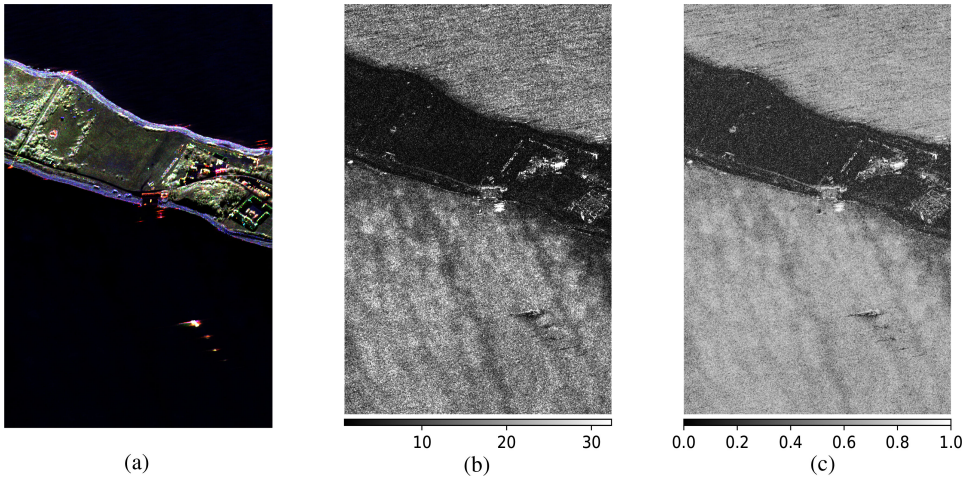

Fig. 10. Scene acquired in the X-band with the F-SAR over Sjaellands Odde. (a) Van Zyl decomposition. The RGB channels correspond to the power explained by, respectively, the even-bounce, the remainder, and the odd-bounce components of the decomposition. (b) $-2\rho_{bd}\ln(Q_{bd})$ after applying the rotations to the covariance matrix. (c) $|\rho_{rrll}|$.

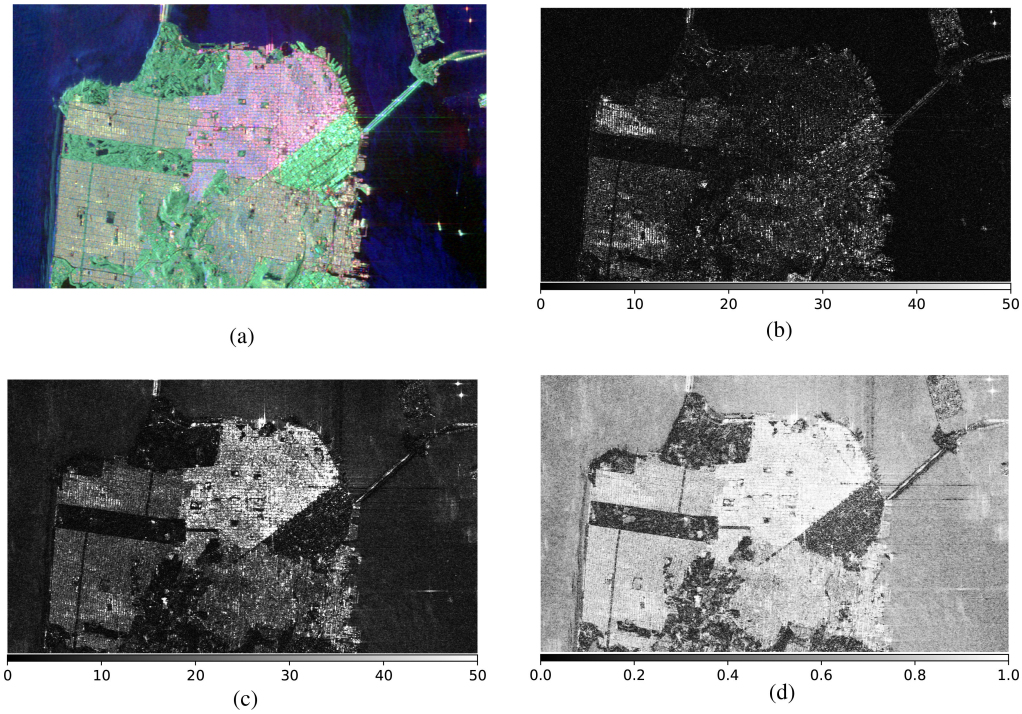

Fig. 11. (a) RGB image of the area obtained with the van Zyl decomposition. The RGB channels correspond to the logarithm of the power explained by double-bounce, volume, and single-bounce scattering according to the decomposition proposed by van Zyl. (b) $-2\rho_{bd}\ln(Q_{bd})$ over the scene, prior to any covariance matrix rotation. (c) $-2\rho_{bd}\ln(Q_{bd})$ after rotation of the covariance matrices. (d) $|\rho_{rrll}|$.

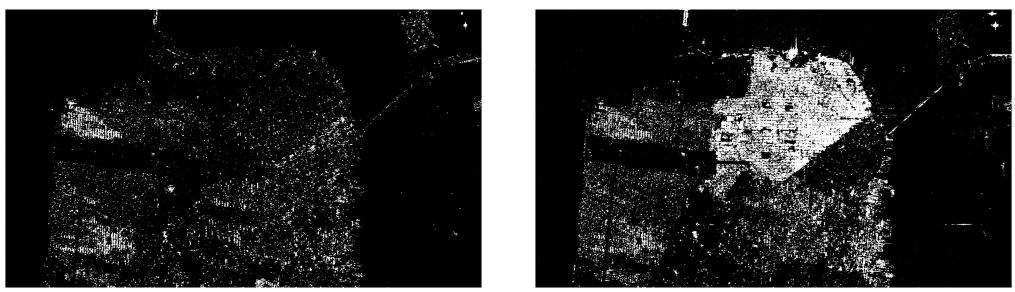

Fig. 12. (a) Detection obtained with the block-diagonal test statistic before rotations to the covariance matrices with a false alarm rate $\alpha = 10^{-3}$. (b) Detection obtained with the same parameters, after rotation of the covariance matrices.

Fig. 13. Combined detection using both detection results from Fig. 12.

covariance matrices, are shown Fig. 12. The combination of these two detections is shown Fig. 13.

IV. Conclusion

In this article, two test statistics for reflection symmetry are presented, together with their associated distributions in case of reflection symmetry. One is an *ad hoc* adaptation of a change detection algorithm, while the second is a novel algorithm based on a block-diagonality test with a CFAR property for reflection asymmetry detection.

Their application to quad-polarimetric data over urban areas show that these tests highlight buildings and urban areas which are rotated compared to the radar LOS. With proper rotations applied to the covariance matrix, the dependence of reflection symmetry on the orientation of objects on the ground can be partially removed, and these tests can also be used to highlight buildings aligned with the radar LOS. After these rotations, however, structures rotated with a large azimuth angle might not be detected if they do not correspond to a rotated dihedral scattering, which can happen in densely built urban areas. The combined use of the test statistics before and after applying the orientation correction with a bias makes it possible to highlight buildings aligned and not aligned with the radar LOS. Furthermore, after the proposed rotations are applied, the test statistics show the same patterns as the amplitude of the correlation coefficient $|\rho_{rrll}|$, as they highlight similar features. The two presented test statistics give excellent results with reduced noise on the background when compared to the latter. Furthermore, testing for a hypothesis on a pixel basis is faster than comparing a pixel's value to its surroundings and makes the test more robust to borders between different types of ground cover. The results obtained on the high-resolution data acquired by the F-SAR demonstrate the potential of these tests for building detection embedded in natural backgrounds, which is of interest for potential military applications.

The roughness of the sea surface at low wavelengths such as X-band makes it difficult to detect ships at sea. However, these tests also show some potential for ship detection at L-band and longer wavelengths. These are not the only possible applications of tests for reflection symmetry, and further work is necessary to evaluate their usefulness on other topics such as classification or image segmentation.

Appendix A

Proof: We consider a p-component vector $\boldsymbol{X} \sim N_{\mathbb{C}}(\boldsymbol{\mu},\ \boldsymbol{\Sigma})$ partitioned into t subvectors of dimensions $p_1, \ldots, p_t$ with parameters partitioned similarly

$$\boldsymbol{X} = \begin{bmatrix} \boldsymbol{X}^{(1)} \\ \boldsymbol{X}^{(2)} \\ \vdots \\ \boldsymbol{X}^{(t)} \end{bmatrix}$$

$$\boldsymbol{\mu} = \begin{bmatrix} \boldsymbol{\mu}^{(1)} \\ \boldsymbol{\mu}^{(2)} \\ \vdots \\ \boldsymbol{\mu}^{(t)} \end{bmatrix}$$

$$\boldsymbol{\Sigma} = \begin{bmatrix} \boldsymbol{\Sigma}_{11} & \boldsymbol{\Sigma}_{12} & \ldots & \boldsymbol{\Sigma}_{1t} \\ \boldsymbol{\Sigma}_{21} & \boldsymbol{\Sigma}_{22} & \ldots & \boldsymbol{\Sigma}_{2t} \\ \vdots & \vdots & & \vdots \\ \boldsymbol{\Sigma}_{t1} & \boldsymbol{\Sigma}_{t2} & \ldots & \boldsymbol{\Sigma}_{tt} \end{bmatrix}.$$

We consider m independent observations $\boldsymbol{X}_1, \ldots,\ \boldsymbol{X}_m$ of $\boldsymbol{X}$ and want to test the hypothesis that the t components are independent, i.e.

$$\mathcal{H}_0 : \boldsymbol{\Sigma}_{ij} = \boldsymbol{0} \text{ for } i \neq j$$

$$\mathcal{H}_1 : \exists i \neq j \text{ for which } \boldsymbol{\Sigma}_{ij} \neq \boldsymbol{0}.$$

We define

$$\begin{aligned} \boldsymbol{A} &= \sum_{j=1}^{m} (\boldsymbol{X}_j - \bar{\boldsymbol{X}})(\boldsymbol{X}_j - \bar{\boldsymbol{X}})^{*T} \\ &= m\widehat{\boldsymbol{\Sigma}} \\ &\sim W_{\mathbb{C}}\,(p, m-1, \boldsymbol{\Sigma}) \end{aligned}$$

where $\bar{\boldsymbol{X}}$ is the average of the observations $\boldsymbol{X}_1, \ldots, \boldsymbol{X}_m$. For the partitioning

$$\boldsymbol{A} = \begin{bmatrix} \boldsymbol{A}_{11} & \boldsymbol{A}_{12} & \ldots & \boldsymbol{A}_{1t} \\ \boldsymbol{A}_{21} & \boldsymbol{A}_{22} & \ldots & \boldsymbol{A}_{2t} \\ \vdots & \vdots & & \vdots \\ \boldsymbol{A}_{t1} & \boldsymbol{A}_{t2} & \ldots & \boldsymbol{A}_{tt} \end{bmatrix}$$

we get

$$\boldsymbol{A}_{\tau\tau} \sim W_{\mathbb{C}}\,(p_{\tau\tau}, m-1, \boldsymbol{\Sigma}_{\tau\tau}),\ \tau = 1,\ \ldots,\ t.$$

According to, e.g., [24], the likelihood ratio test statistic for testing H_0 is

$$\Lambda_1 = \left(\frac{\det \boldsymbol{A}}{\prod_{\tau=1}^{t} \det \mathbf{A}_{\tau\tau}} \right)^{m}.$$

The result on Q follows by a reformulation of this.

According [24], we furthermore have that the expected value of Λ_1^h is

$$\mathrm{E}(\Lambda_1^h) = \prod_{\tau=1}^{t-1} \prod_{j=1}^{p_\tau} \frac{\Gamma(m-j)\Gamma(m-q_\tau-j+mh)}{\Gamma(m-q_\tau-j)\Gamma(m-j+mh)}$$

and thus the expected value of Q^h is

$$\begin{aligned}\mathrm{E}(Q^h) &= \mathrm{E}\left(\Lambda_1^{h\times n/(n+1)}\right)\\ &= \prod_{\tau=1}^{t-1}\prod_{j=1}^{p_\tau}\frac{\Gamma(n+1-j)}{\Gamma(n+1-q_\tau-j)}\\ &\quad\frac{\Gamma(n(1+h)-q_\tau-j+1)}{\Gamma(n(1+h)-j+1)}\end{aligned}$$

where

$$q_k = p_{k+1}+\cdots+p_t, \qquad k=1,\ldots,\,t-1.$$

For $t=3$, the terms depending on h may be written

$$\begin{aligned}&\prod_{j=1}^{p_1}\frac{\Gamma(n(1+h)-q_1-j+1)}{\Gamma(n(1+h)-j+1)}\\ &\prod_{j=1}^{p_2}\frac{\Gamma(n(1+h)-q_2-j+1)}{\Gamma(n(1+h)-j+1)}\\ &=\frac{\prod_{k=1}^{p_1}\Gamma(n(1+h)-q_1-k+1)}{\prod_{j=1}^{p_1}\Gamma(n(1+h)-j+1)}\\ &\frac{\prod_{k=p_1+1}^{p_1+p_2}\Gamma(n(1+h)-q_2+p_1-k+1)}{\prod_{j=p_1+1}^{p_2+p_1}\Gamma(n(1+h)+p_1-j+1)}.\end{aligned}$$

We now apply the approximations given in the theorem by [25] and use the notation used in the version presented in [19]. There we also provide some useful formulas on sums of Bernoulli polynomials. Thus

$$\begin{aligned}a &= p_1+p_2\\ b &= p_1+p_2\\ x_k &= n\\ y_j &= n\\ \beta_k &= \beta = n\,(1-\rho)\\ \varepsilon_j &= \varepsilon = n\,(1-\rho)\end{aligned}$$

$$\begin{aligned}&\xi_k = -q_1-k+1, \qquad k=1,\ldots,\,p_1\\ &\xi_k = -q_2+p_1-k+1, \quad k=p_1+1,\ldots,\,p_1+p_2\\ &\eta_j = -j+1, \qquad j=1,\ldots,\,p_1\\ &\eta_j = p_1-j+1, \qquad j=p_1+1,\ldots,\,p_1+p_2\end{aligned}$$

$$\begin{aligned}f &= -2\left[\sum_{k=1}^{p_1+p_2}\xi_k-\sum_{j=1}^{p_1+p_2}\eta_j-\frac{1}{2}(a-b)\right]\\ &= -2\left[\sum_{k=1}^{p_1+p_2}(\xi_k-\eta_k)\right]\\ &= 2\,[p_1q_1+p_2q_2]\\ &= 2\,[p_1p_2+p_1p_3+p_2p_3]\\ &= p^2-\sum_{\tau=1}^{3}p_\tau^2.\end{aligned}$$

For convenience, we also introduce

$$\begin{aligned}u_1 &= n\,(1-\rho)\\ v_1 &= n\,(1-\rho)-q_1 = u_1-q_1\\ u_2 &= n\,(1-\rho)+p_1 = u_1+p_1\\ v_2 &= n\,(1-\rho)+p_1-q_2 = u_2-q_2.\end{aligned}$$

We only consider the case $t=3$. The case $t=2$ is treated similarly, and the expressions are generally simpler. We define ω_1 by the expression

$$\begin{aligned}2n\rho\omega_1 &= \sum_{k=1}^{p_1+p_2}B_2\,(\beta_k+\xi_k)-\sum_{j=1}^{p_1+p_2}B_2\,(\varepsilon_j+\eta_j)\\ &= \sum_{k=1}^{p_1+p_2}\{B_2\,(\beta_k+\xi_k)-B_3\,(\varepsilon_k+\eta_k)\}\\ &= \sum_{k=1}^{p_1}\{B_2\,(v_1-k+1)-B_2\,(u_1-k+1)\}\\ &\quad+\sum_{k=p_1+1}^{p_1+p_2}\{B_2\,(v_2-k+1)-B_2\,(u_2-k+1)\}\\ &= \{v_1-u_1\}\left\{p_1[v_1+u_1]-2\sum_{k=1}^{p_1}B_1(k)\right\}\\ &\quad+\{v_2-u_2\}\left\{p_2[v_2+u_2]-2\sum_{k=p_1+1}^{p_1+p_2}B_1(k)\right\}\\ &= -q_1\left\{p_1[2\beta-q_1]-p_1^2\right\}\\ &\quad-q_2\left\{p_2[2\beta+2p_1-q_2]-p_2(2p_1+p_2)\right\}\\ &= -\left\{p^2-\sum_{\tau=1}^{3}p_\tau^2\right\}\beta+\frac{1}{3}\left\{p^3-\sum_{\tau=1}^{3}p_\tau^3\right\}.\end{aligned}$$

If this term is put equal to 0, we have

$$\beta = n\,(1-\rho) = \frac{1}{3}\frac{p^3-\sum_{\tau=1}^{3}p_\tau^3}{p^2-\sum_{\tau=1}^{3}p_\tau^2}$$

or

$$\rho = 1-\frac{1}{3n}\frac{p^3-\sum_{\tau=1}^{3}p_\tau^3}{p^2-\sum_{\tau=1}^{3}p_\tau^2}.$$

We now define ω_2 by the expression

$$\begin{aligned}-6n\rho^2\omega_2 &= \sum_{k=1}^{p_1+p_2}\left\{B_3\,(\beta_k+\xi_k)-\sum_{j=1}^{p_1+p_2}B_3\,(\varepsilon_j+\eta_j)\right\}\\ &= \sum_{k=1}^{p_1}\Big\{B_3\,(n\,(1-\rho)-q_1-k+1)\\ &\quad-B_3\,(n\,(1-\rho)-k+1)\Big\}\\ &\quad\sum_{k=p_1+1}^{p_1+p_2}\Big\{B_3\,(n\,(1-\rho)+p_1-q_2-k+1)\\ &\quad-B_3\,(n\,(1-\rho)+p_1-k+1)\Big\}.\end{aligned}$$

The two terms are

$$\begin{aligned}T_1 =\ & \{v_1-u_1\}\left\{p_1[v_1^2+v_1u_1+u_1^2]\right.\\ & \left.-3\,(v_1+u_1)\sum_{k=1}^{p_1}B_1(k)+3\sum_{k=1}^{p_1}B_2(k)\right\}\\ =\ & -q_1\left\{p_1[v_1^2+v_1u_1+u_1^2]-\frac{3}{2}\,(v_1+u_1)\,p_1^2\right.\\ & \left.+\frac{1}{2}p_1(2p_1^2-1)\right\}\\ =\ & -p_1(p_2+p_3)\left\{3\beta^2-3p\beta+(p_2+p_3)^2\right.\\ & \left.+\frac{3}{2}p_1(p_2+p_3)+p_1^2-\frac{1}{2}\right\}\end{aligned}$$

$$\begin{aligned}T_2 =\ & \{v_2-u_2\}\left\{p_2[v_2^2+v_2u_2+u_2^2]\right.\\ & \left.-3\,(v_2+u_2)\sum_{k=p_1+1}^{p_1+p_2}B_1(k)+3\sum_{k=p_1+1}^{p_1+p_2}B_2(k)\right\}\\ =\ & -q_2\left\{p_2[v_2^2+v_2u_2+u_2^2]-\frac{3}{2}\,(v_2+u_2)\,p_2(2p_1+p_2)\right.\\ & \left.+3p_2(p_1^2+p_1p_2+\frac{1}{3}p_2^2-\frac{1}{6})\right\}\\ =\ & -p_2p_3\left\{3\beta^2-3\,(p_2+p_3)\,\beta+p_2^2+p_3^2+\frac{3}{2}p_2p_3-\frac{1}{2}\right\}.\end{aligned}$$

Thus

$$\begin{aligned}6n^2\rho^2\omega_2 =\ & 3\{p_1p_2+p_1p_3+p_2p_3\}\beta^2\\ & -3\left\{p_1p_2^2+p_1^2p_2+p_1p_3^2+p_1^2p_3\right.\\ & \left.+p_2p_3^2+p_2^2p_3+2p_1p_2p_3\right\}\beta\\ & +\left\{p_1p_2^3+p_1^3p_2+p_1p_3^3\right.\\ & \left.+p_1^3p_3+p_2p_3^3+p_2^3p_3\right\}\\ & +\frac{3}{2}\{p_1^2p_2^2+p_1^2p_3^2+p_2^2p_3^2\}\\ & +3\{p_1p_2p_3^2+p_1p_2^2p_3+p_1^2p_2p_3\}\\ =\ & \frac{3}{2}\left\{p^2-\sum_{\tau=1}^{3}p_\tau^2\right\}\beta^2-\left\{p^3-\sum_{\tau=1}^{3}p_\tau^3\right\}\beta\\ & +\frac{1}{4}\left\{p^4-\sum_{\tau=1}^{3}p_\tau^4\right\}\\ =\ & -\frac{1}{6}\frac{\left\{p^3-\sum_{\tau=1}^{3}p_\tau^3\right\}^2}{p^2-\sum_{\tau=1}^{3}p_\tau^2}+\frac{1}{4}\left\{p^4-\sum_{\tau=1}^{3}p_\tau^4\right\}\end{aligned}$$

or

$$\begin{aligned}\omega_2=\frac{1}{n^2\rho^2}\Bigg[& -\frac{1}{36n^2\rho^2}\frac{\left\{p^3-\sum_{\tau=1}^{3}p_\tau^3\right\}^2}{p^2-\sum_{\tau=1}^{3}p_\tau^2}\\ & +\frac{1}{24n^2\rho^2}\left\{p^4-\sum_{\tau=1}^{3}p_\tau^4\right\}\Bigg].\end{aligned}$$

This proves the theorem.

ACKNOWLEDGMENT

The authors would like to express their sincere thanks to DALO and Terma for letting us use data from the F-SAR data collection campaigns which they co-financed, as well as the reviewers for their comments and suggestions.

REFERENCES

[1] M. di Bisceglie and C. Galdi, "CFAR detection of extended objects in high-resolution SAR images," *IEEE Trans. Geosci. Remote Sens.*, vol. 43, no. 4, pp. 833–843, 2005.

[2] L. M. Novak, M. B. Sechtin, and M. J. Cardullo, "Studies of target detection algorithms that use polarimetric radar data," *IEEE Trans. Aerosp. Electron. Syst.*, vol. 25, no. 2, pp. 150–165, Mar. 1989.

[3] A. Marino, S. R. Cloude, and I. H. Woodhouse, "A polarimetric target detector using the Huynen fork," *IEEE Trans. Geosci. Remote Sens.*, vol. 48, no. 5, pp. 2357–2366, May 2010.

[4] L. Ferro-Famil and E. Pottier, "Urban area remote sensing from L-band polSAR data using time-frequency techniques," in *Proc. IEEE Urban Remote Sens. Joint Event*, 2007, pp. 1–6.

[5] M. Borgeaud, R. T. Shin, and J. A. Kong, "Theoretical models for polarimetric radar clutter," *J. Electromagn. Waves Appl.*, vol. 1, no. 1, pp. 73–89, 1987.

[6] S. Nghiem, S. Yueh, R. Kwok, and F. Li, "Symmetry properties in polarimetric remote sensing," *Radio Sci.*, vol. 27, no. 5, pp. 693–711, 1992.

[7] V. Alberga, G. Satalino, and D. Staykova, "Comparison of polarimetric SAR observables in terms of classification performance," *Int. J. Remote Sens.*, vol. 29, no. 14, pp. 4129–4150, 2008.

[8] A. Freeman and S. L. Durden, "A three-component scattering model for polarimetric SAR data," *IEEE Trans. Geosci. Remote Sens.*, vol. 36, no. 3, pp. 963–973, May 1998.

[9] J. J. van Zyl, "Application of Cloude's target decomposition theorem to polarimetric imaging radar data," in *Proc. Radar Polarimetry, Int. Soc. Opt. Photon.*, 1993, pp. 184–191.

[10] M. Arii, H. Yamada, S. Kojima, and M. Ohki, "Sensitivity analysis of multifrequency MIMP SAR data from rice paddies," *IEEE Trans. Geosci. Remote Sens.*, vol. 57, no. 6, pp. 3543–3551, Jun. 2019.

[11] Y. Yamaguchi, T. Moriyama, M. Ishido, and H. Yamada, "Four-component scattering model for polarimetric SAR image decomposition," *IEEE Trans. Geosci. Remote Sens.*, vol. 43, no. 8, pp. 1699–1706, Aug. 2005.

[12] E. Krogager, "New decomposition of the radar target scattering matrix," *Electron. Lett.*, vol. 26, no. 18, pp. 1525–1527, 1990.

[13] J.-S. Lee, D. L. Schuler, T. L. Ainsworth, E. Krogager, D. Kasilingam, and W.-M. Boerner, "On the estimation of radar polarization orientation shifts induced by terrain slopes," *IEEE Trans. Geosci. Remote Sens.*, vol. 40, no. 1, pp. 30–41, Jan. 2002.

[14] N. Wang, G. Shi, L. Liu, L. Zhao, and G. Kuang, "Polarimetric SAR target detection using the reflection symmetry," *IEEE Geosci. Remote Sens. Lett.*, vol. 9, no. 6, pp. 1104–1108, 2012.

[15] T. Ainsworth, D. Schuler, and J.-S. Lee, "Polarimetric SAR characterization of man-made structures in urban areas using normalized circular-pol correlation coefficients," *Remote Sens. Environ.*, vol. 112, no. 6, pp. 2876–2885, 2008.
[16] D. Duan, Y. Wang, and H. Li, "A descriptor to separate urban targets with large azimuth orientation angles from vegetation targets in polSAR data," in *Proc. IEEE Int. Geosci. Remote Sens. Symp.*, 2021, pp. 5425–5428.
[17] L. Pallotta, A. De Maio, and D. Orlando, "A robust framework for covariance classification in heterogeneous polarimetric SAR images and its application to L-band data," *IEEE Trans. Geosci. Remote Sens.*, vol. 57, no. 1, pp. 104–119, Jan. 2019.
[18] W. An and M. Lin, "An incoherent decomposition algorithm based on polarimetric symmetry for multilook polarimetric SAR data," *IEEE Trans. Geosci. Remote Sens.*, vol. 58, no. 4, pp. 2383–2397, Apr. 2020.
[19] K. Conradsen, A. A. Nielsen, J. Schou, and H. Skriver, "A test statistic in the complex Wishart distribution and its application to change detection in polarimetric sar data," *IEEE Trans. Geosci. Remote Sens.*, vol. 41, no. 1, pp. 4–19, Jan. 2003.
[20] S. N. Anfinsen, A. P. Doulgeris, and T. Eltoft, "Estimation of the equivalent number of looks in polarimetric synthetic aperture radar imagery," *IEEE Trans. Geosci. Remote Sens.*, vol. 47, no. 11, pp. 3795–3809, Nov. 2009.
[21] M. Sugimoto, K. Ouchi, and Y. Nakamura, "Four-component scattering power decomposition algorithm with rotation of covariance matrix using ALOS-PALSAR polarimetric data," *Remote Sens.*, vol. 4, no. 8, pp. 2199–2209, 2012.
[22] J.-S. Lee, D. L. Schuler, and T. L. Ainsworth, "Polarimetric SAR data compensation for terrain azimuth slope variation," *IEEE Trans. Geosci. Remote Sens.*, vol. 38, no. 5, pp. 2153–2163, Sep. 2000.
[23] J. M. Delgado Blasco, M. Fitrzyk, J. Patruno, A. M. Ruiz-Armenteros, and M. Marconcini, "Effects on the double bounce detection in urban areas based on SAR polarimetric characteristics," *Remote Sens.*, vol. 12, no. 7, 2020, Art. no. 1187.
[24] C. A. Coelho, B. C. Arnold, and F. J. Marques, "The exact and near-exact distributions of the main likelihood ratio test statistics used in the complex multivariate normal setting," *Test*, vol. 24, no. 2, pp. 386–416, 2015.
[25] G. E. Box, "A general distribution theory for a class of likelihood criteria," *Biometrika*, vol. 36, no. 3/4, pp. 317–346, 1949.

Paul Connetable received the M.Sc. degrees, in 2017, from the Ecole Centrale Nantes, Nantes, France and from the Technical University of Denmark, Kongens Lyngby, Denmark, where he is currently working toward the Ph.D. degree.

His research interests include the application of statistics to polarimetric SAR images and the detection and classification of man-made structures in polarimetric SAR images.

Knut Conradsen received the Candidatus Scientiarum degree in mathematics from the University of Copenhagen, Copenhagen, Denmark, in 1970.

Since 1970, he has been with the Technical University of Denmark (DTU), Kongens Lyngby, Denmark, where he is currently a Professor Emeritus with the Department of Applied Mathematics and Computer Science. From 1995 to 2010, he was a Provost (Deputy Rector) of DTU. His work includes the analysis of multispectral/hyperspectral and multitemporal data, as well as optical radar sensors. His research interests include the application of statistics and statistical models in primarily medical image analysis, remote sensing, and industrial applications.

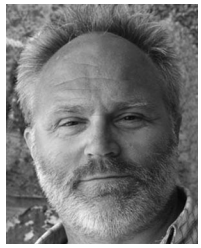

Allan Aasbjerg Nielsen received the M.Sc. and Ph.D. degrees from the Technical University of Denmark (DTU), Kongens Lyngby, Denmark, in 1978 and 1994, respectively.

From 1977 to 1978, he was with the Danish Defense Research Establishment. From 1978 to 1985, he was with the Thermal Insulation Laboratory, DTU, where her worked on energy conservation in housing. He was with the Section for Image Analysis and Section for Geoinformatics, Department of Informatics and Mathematical Modeling, DTU from 1985 to 2001 and 2001 to 2006, respectively. From 2007 to 2013, he was with the Danish National Space Center's Section for Geodesy. From 2013 to 2020, he was an Associate Professor with the Department of Applied Mathematics and Computer Science, DTU, where he is currently Emeritus. Since 1985, he has worked on several national and international projects on the development, implementation, and application of statistical methods, and remote sensing in mineral exploration, mapping, geology, agriculture, environmental monitoring, oceanography, geodesy, and security funded by industry, the European Union, the Danish International Development Agency (Danida), and the Danish National Research Councils.

Henning Skriver (Member, IEEE) received the M.Sc. and Ph.D. degrees in electrical engineering from the Technical University of Denmark (DTU), Kongens Lyngby, Denmark, in 1983 and 1989, respectively.

Since 1983, he has been with DTU, where he is now the Head of the DTU Space Department. His work has been primarily concerned with topics related to the utilization of SAR data for different applications, such as sea ice parameter retrieval from SAR data, as well as different aspects of land applications of SAR data, such as forestry, agricultural, environmental, and topographic mapping applications using both satellite SAR data and data from polarimetric SARs, e.g., the Danish airborne polarimetric SAR, EMISAR, and the German experimental SAR ESAR. His research interests include methods for the processing of SAR data; SAR image simulation; SAR image filtering; speckle statistics; and texture analysis, segmentation, calibration, change detection, classification, and polarimetric analysis and processing.